J Neurophysiol 106: 527–537, 2011.
First published May 11, 2011; doi:10.1152/jn.01127.2010.

NMDA-induced burst firing in a model subthalamic nucleus neuron

Shigeru Kubota[1] and Jonathan E. Rubin[2]

[1]*Graduate School of Science and Engineering, Yamagata University, Yonezawa, Yamagata, Japan; and* [2]*Department of Mathematics, University of Pittsburgh, Pittsburgh, Pennsylvania*

Submitted 27 December 2010; accepted in final form 5 May 2011

Kubota S, Rubin JE. NMDA-induced burst firing in a model subthalamic nucleus neuron. *J Neurophysiol* 106: 527–537, 2011. First published May 11, 2011; doi:10.1152/jn.01127.2010.—Experiments in rat brain slice show that hyperpolarized subthalamic nucleus (STN) neurons engage in slow, regular burst firing when treated with an *N*-methyl-D-aspartate (NMDA) bath. A depolarization-activated inward current (DIC) has been hypothesized to contribute to this bursting activity. To explore the mechanism for STN burst firing in this setting, we augmented a previously published conductance-based computational model for single rat STN neurons to include both DIC and NMDA currents, fit to data from published electrophysiological recordings. Simulations show that with these additions, the model engages in bursting activity at <1 Hz in response to hyperpolarizing current injection and that this bursting exhibits several features observed experimentally in STN. Furthermore, a reduced model is used to show that the combination of NMDA and DIC currents, but not either alone, suffices to generate oscillations under hyperpolarizing current injection. STN neurons show enhanced burstiness in Parkinson's disease patients and experimental models of parkinsonism, and the burst mechanism studied presently could contribute to this effect.

bursting oscillations; *N*-methyl-D-aspartate current; conductance-based models; parkinsonian activity

IN THE SUBTHALAMIC NUCLEUS (STN), an increased incidence of oscillations and burst firing, as well as higher overall spike rates, are observed in experimental (Bergman et al. 1994; Mallet et al. 2008) and clinical parkinsonian states (Brown et al. 2001; Levy et al. 2001; Magnin et al. 2000), relative to normal conditions. These parkinsonian alterations in STN outputs may arise through reciprocal synaptic interactions of STN neurons with neurons in the external segment of the globus pallidus (Bevan et al. 2002a, 2002b; Plenz and Kitai 1999; Smith et al. 1998; Terman et al. 2002). STN neurons also receive glutamatergic inputs from other brain areas, however, including cortical inputs via the so-called hyperdirect pathway (Feger et al. 1997; Magill et al. 2001, 2004a; Mallet et al. 2008; Nambu et al. 1996, 2002), offering an alternative source for the modulation of STN activity. Individual STN neurons can also fire bursts in rat STN slice preparations, particularly under various manipulations such as injection of hyperpolarizing current or *N*-methyl-D-aspartate (NMDA) receptor stimulation (Beurrier et al. 1999; Loucif et al. 2008; Loucif et al. 2005; Overton and Greenfield 1995; Rouzaire-Dubois and Scarnati 1987; Zhu et al. 2004, 2005).

Zhu et al. (2004, 2005) characterized a depolarization-activated inward current (DIC) that contributes to slow (0.4 Hz mean frequency) burst firing in hyperpolarized STN neurons in a rat brain slice bathed with NMDA. They performed a variety of experiments to elucidate the features of the currents and bursting they observed. The DIC itself was activated by calcium (Ca^{2+}) influx specifically through NMDA channels and inactivated by voltage. The presence of sodium (Na^+) in the perfusate was required for DIC expression, suggesting that this is a Ca^{2+}-activated nonselective cationic current. Bursting, or membrane potential oscillations, persisted under application of the Ca^{2+}-activated potassium (K^+) channel blocker apamin or the Na^+ channel blocker tetrodotoxin (TTX), as well as in conditions of low magnesium (Mg^{2+}), which releases NMDA channels from their voltage-dependent block, or low K^+. Activity was lost, however, when Mg^{2+} levels were high or sodium levels were low. Together, these results suggest that hyperpolarized STN neurons can be induced to fire at high frequencies in an NMDA bath due to the combined actions of their NMDA and DIC currents, but they leave open the question of how high-frequency activity is terminated such that bursting oscillations result.

Computational analysis offers an opportunity to explore the mechanisms underlying bursting in individual STN neurons. In this article, we present the results of such a computational study, performed by augmenting an existing conductance-based, single-compartment computational model for an STN neuron (Terman et al. 2002) to include NMDA and DIC currents, fit to the data of Zhu et al. (2005). We characterize the activity of this model under different levels of current injection, with or without NMDA exposure, and show that the model responds to various manipulations in a way that is consistent with experimental observations (Zhu et al. 2005). Notably, we find that without any additional parameter tuning, the combined effects of hyperpolarizing current injection, the NMDA current, and the DIC current are sufficient to yield STN bursting that is consistent with the experimental results of Zhu et al. (2004), without invoking any additional currents or other features. We also present a reduced model that includes only these minimal components to illustrate the fundamental features of the underlying oscillation, and we discuss the possible relevance of these results to parkinsonian conditions.

METHODS

STN neuron model. We constructed a conductance-based STN neuron to analyze activity patterns resulting from NMDA application. We incorporated the active currents used in the STN neuron model of Terman et al. (2002), which exhibits firing properties characteristic of rat STN neurons observed in in vitro recordings (Beurrier et al. 2000; Bevan and Wilson 1999; Bevan et al. 2000): voltage-dependent Na^+/K^+ currents (I_{Na} and I_K), a low-threshold T-type Ca^{2+} current (I_T), a high-threshold Ca^{2+} current (I_{Ca}), and a Ca^{2+}-activated K^+ current (I_{AHP}) (Appendix). Furthermore, we developed a model of the NMDA receptor (NMDAR)-mediated currents (I_{NMDA}) and DIC (I_{DIC}) that were measured in whole cell patch recordings in rat brain

Address for reprint requests and other correspondence: J. Rubin, Dept. of Mathematics, Univ. of Pittsburgh, 301 Thackeray Hall, Pittsburgh, PA 15260 (e-mail: rubin@math.pitt.edu).

slices (Zhu et al. 2004, 2005). The membrane potential (V) of our neuron model obeys

$$C_m \frac{dV}{dt} = -I_{leak} - I_{Na} - I_K - I_T - I_{Ca} - I_{AHP} - I_{NMDA} - I_{DIC} + I_{inj}, \quad (1)$$

where $C_m = 1\ \mu F/cm^2$ is the specific membrane capacitance; the leak current $I_{leak} = g_l(V - V_l)$ with the leak conductance $g_l = 2.25$ mS/cm^2 and the leak reversal potential $V_l = -60$ mV (Terman et al. 2002); and I_{inj} is the injected current. Other currents have been characterized in STN neurons (Atherton et al. 2010; Barraza et al. 2009; Beurrier et al. 1999; Gillies and Willshaw 2006; Hahn and McIntyre 2010; Overton and Greenfield 1995; Nakanishi et al. 1987), but since they were found not to be necessary for the reproduction of the experimental results that we studied (Zhu et al. 2004, 2005), they were omitted from the model.

Functional NMDARs are heterotetramers consisting of obligatory NR1 subunits and modulatory NR2 (NR2A–NR2D) subunits. The NMDARs in STN neurons appear to mainly comprise NR2D-containing NMDARs, which are expressed in quite limited regions in the adult brain (Monyer et al. 1994; Standaert et al. 1994; Wenzel et al. 1996). NMDARs having NR2D subunits are characterized by a voltage dependence provided by Mg^{2+} block, which is weaker than that of cortical NMDARs containing NR2A and NR2B subunits, and also by strong Ca^{2+}-dependent desensitization (Krupp et al. 1996; Monyer et al. 1994). Therefore, we consider that the conductance of the NMDA current depends on the membrane voltage and, additionally, that the kinetics of channel opening relies on the mechanism of NMDA-induced activation as well as Ca^{2+}-dependent inactivation. With this assumption, the NMDA current can be described as follows:

$$I_{NMDA} = G_{NMDA}(V, m_N, h_N)(V - V_N), \quad (2)$$

$$G_{NMDA}(V, m_N, h_N) = \frac{g_N m_N h_N}{1 + \eta[Mg]\exp(-\gamma V)}, \quad (3)$$

$$\frac{dh_N}{dt} = \frac{-h_N + h_N^{\infty}([Ca]_N)}{\tau_{h_N}}. \quad (4)$$

The peak conductance $g_N = 20$ mS/cm^2 unless otherwise stated, $V_N = -20$ mV is the reversal potential (Zhu et al. 2005), [Mg] = 1.3 mM is the Mg^{2+} ion concentration (Zhu et al. 2005), $\eta = 0.33\ mM^{-1}$, and $\gamma = 0.05\ mV^{-1}$ (Jahr and Stevens 1990). The voltage dependence in *Eq. 3* is modified from Jahr and Stevens (1990) to reproduce the data of in vitro STN cells (Zhu et al. 2005; Fig. 1). The activation variable m_N is set to 1, unless otherwise stated, to reproduce the experimental conditions of Zhu et al. (2004, 2005) using bath application of NMDA with a constant concentration. The inactivation variable h_N evolves according to *Eq. 4*, where $h_N^{\infty}([Ca]_N) = 1/\{1 + \exp[([Ca]_N - \theta_h^N)/\sigma_h^N]\}$ is a decreasing function of the NMDAR-mediated Ca^{2+} concentration, $[Ca]_N$ (Fig. 1*A*), and the inactivation time constant $\tau_{h_N} = 3{,}000$ ms (Krupp et al. 1996). The Ca^{2+} dynamics related to NMDAR inactivation is described by the first-order kinetics:

$$\frac{d[Ca]_N}{dt} = \frac{-[Ca]_N - I_{NMDA}^{Ca}}{\tau_{CaN}}, \quad (5)$$

where the Ca^{2+} influx through NMDARs is $I_{NMDA}^{Ca} = k_1^N G_{NMDA}(V, m_N, h_N)(V - V_{Ca})$, the time constant $\tau_{CaN} = 80$ ms, and the parameters $k_1^N = 0.005$ and $V_{Ca} = 120$ mV (Terman et al. 2002). This model reflects experimental findings (Zhu et al. 2005) suggesting that the

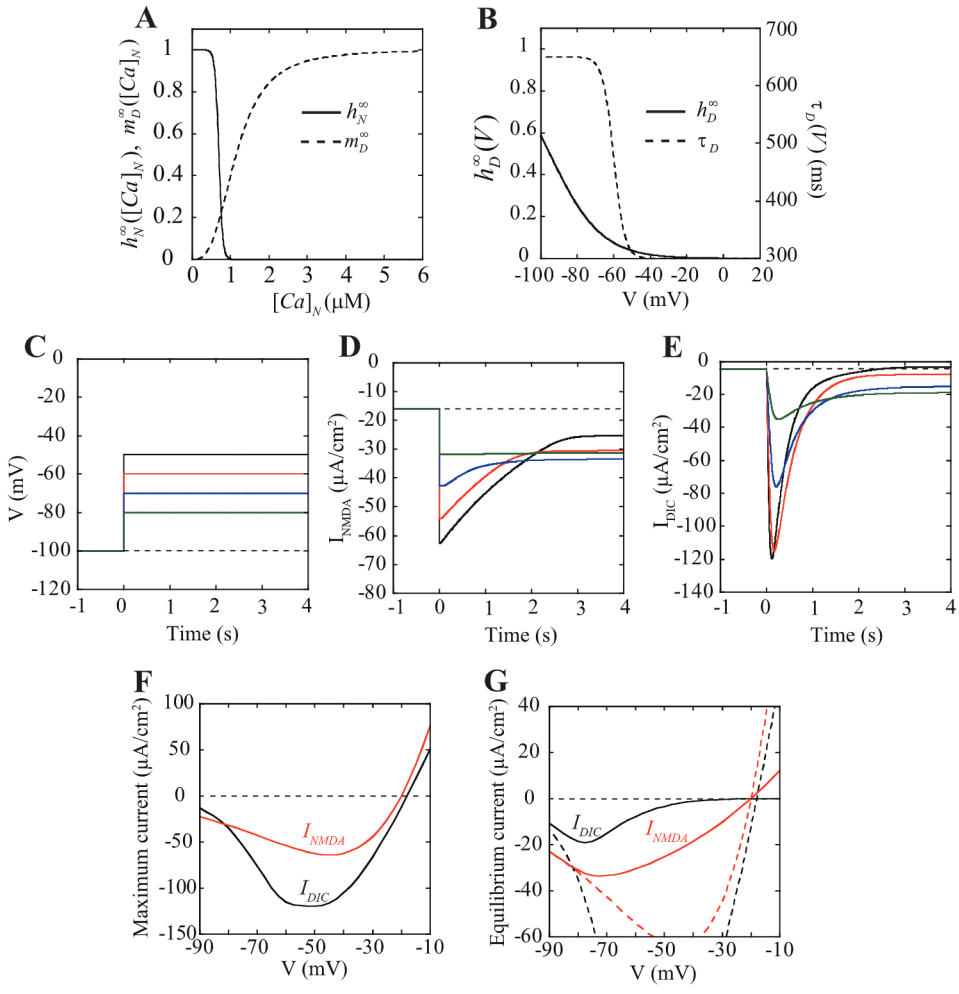

Fig. 1. Characteristics of the depolarization-induced current (DIC) and the NMDA current. *A*: Ca^{2+} concentration dependence at the equilibrium state of the activation variable for DIC (m_D^{∞}, dashed line) and of the inactivation variable for NMDA currents (h_N^{∞}, solid line). *B*: voltage dependence of the steady-state inactivation variable (h_D^{∞}, solid line) and its time constant (τ_D, dashed line) for DIC. *C*: membrane potential (V) is depolarized to a value of −50 (black line), −60 (red line), −70 (blue line), or −80 mV (green line) from an initial holding potential of −100 mV. *D*: time course of NMDA current. *E*: time course of DIC. Time courses are displayed with the same color coding used in *C*. *F*: maximum values of NMDA current (red line) and DIC (black line) in response to depolarizing steps to the voltage levels shown on the horizontal axis. *G*: steady-state values of NMDA current (red line) and DIC (black line) in response to the same depolarizing steps. Dashed line shows the maximum values for comparison (as in *F*). Parameter values for all simulations are peak conductances $g_N = 13$ mS/cm^2 and $g_D = 14$ mS/cm^2.

inactivation of the NMDA current depends on the increase in intracellular Ca^{2+} mediated specifically by NMDARs (but not T-, L-, or N-type voltage-gated Ca^{2+} channels).

The same set of experiments indicate that prolonged hyperpolarization (e.g., at $V \sim -100$ mV) strongly activates DIC in a calcium-dependent way, whereas the subsequent depolarization to a fixed holding voltage slowly inactivates it, with inactivation kinetics dependent on the holding voltage. To incorporate these experimental observations, we modeled DIC as follows:

$$I_{\mathrm{DIC}} = g_D m_D^{\infty}([\mathrm{Ca}]_N) h_D (V - V_D). \quad (6)$$

In *Eq. 6*, the peak conductance g_D is set to 20 mS/cm^2 unless otherwise stated, the activation variable depends on the NMDAR-mediated Ca^{2+} concentration, $m_D^{\infty}([\mathrm{Ca}]_N) = ([\mathrm{Ca}]_N)^3/[([\mathrm{Ca}]_N)^3 + k_{\mathrm{d}}^3]$ (Fig. 1*A*) with $k_{\mathrm{d}} = 1.15$ μM, and the reversal potential $V_D = -18$ mV (Zhu et al. 2005). The inactivation variable h_D obeys the following equation:

$$\frac{\mathrm{d}h_D}{\mathrm{d}t} = \frac{-h_D + h_D^{\infty}(V)}{\tau_D(\mathrm{V})}, \quad (7)$$

where the steady-state value and the time constant of h_D are $h_D^{\infty}(V) = 1/\{1 + \exp[(V - \theta_D)/\sigma_D]\}$ and $\tau_D(V) = \tau_D^0 + \tau_D^1/\{1 + \exp[(V - \theta_{\mathrm{D}}^{\tau})/\sigma_D^{\tau}]\}$, respectively (Fig. 1*B*). The parameter values for I_{DIC} and I_{NMDA} that are not mentioned above are summarized as follows: $\theta_h^N = 0.7$ μM, $\sigma_h^N = 0.05$ μM, $\tau_D^0 = 300$ ms, $\tau_D^1 = 350$ ms, $\theta_D = -95$ mV, $\sigma_D = 14$ mV, $\theta_D^{\tau} = -60$ mV, and $\sigma_D^{\tau} = 3$ mV. These values were selected to reproduce the response of STN neurons and their membrane currents observed in the in vitro recordings (Zhu et al. 2004, 2005), i.e., the voltage and hyperpolarization dependence of I_{DIC} and I_{NMDA} (Fig. 1, *C–G*) and the effects of specific ion channel blockers on the firing pattern (Figs. 2 and 3; see RESULTS). All other parameter values and functions included in the model were taken from Terman et al. (2002), with a small number of adjustments, and are described in the APPENDIX.

The neuron model was coded either in C++ programming language or for compilation by XPPAUT software (Ermentrout 2002) and integrated using the fourth-order Runge-Kutta method with the standard time step size of 0.05 ms. XPPAUT was also used for bifurcation analysis (see Fig. 6).

Three-compartment model. Since NMDA channels are located at dendritic sites, to explore the interaction of dendritic oscillations at the soma, we also constructed a three-compartment STN neuron model consisting of two dendritic compartments coupled electrically (with coupling strength scaled appropriately by membrane area) to a common somatic compartment. We included NMDA currents and DIC in the dendritic compartments but not the somatic one; for simplicity, all other currents were the same in all three compartments, with parameters as in the single-compartment model, and we neglected propagation delays. With this assumption, the membrane potentials V_{s} and $V_{\mathrm{d},i}$ ($i = 1, 2$), of the somatic and two dendritic compartments, obey the following equations:

$$C_{\mathrm{m}}\frac{\mathrm{d}V_{\mathrm{s}}}{\mathrm{d}t} = -I_{\mathrm{leak}} - I_{\mathrm{Na}} - I_{\mathrm{K}} - I_{\mathrm{T}} - I_{\mathrm{Ca}} - I_{\mathrm{AHP}} + I_{\mathrm{inj}} + \sum_{i=1}^{2} \frac{g_{\mathrm{c},i}}{p_{\mathrm{s}}}(V_{\mathrm{d},i} - V_{\mathrm{s}}), \quad (8)$$

$$C_{\mathrm{m}}\frac{\mathrm{d}V_{\mathrm{d},i}}{\mathrm{d}t} = -I_{\mathrm{leak}} - I_{\mathrm{Na}} - I_{\mathrm{K}} - I_{\mathrm{T}} - I_{\mathrm{Ca}} - I_{\mathrm{AHP}} - I_{\mathrm{NMDA}} - I_{\mathrm{DIC}} + I_{\mathrm{inj}} + \frac{g_{\mathrm{c},i}}{p_{\mathrm{d},i}}(V_{\mathrm{s}} - V_{\mathrm{d},i}), \quad (9)$$

where $g_{\mathrm{c},i}$ denotes the coupling conductance between the soma and the ith dendrite and is set to $g_{\mathrm{c},1} = g_{\mathrm{c},2} = 1$ mS/cm^2. $p_{\mathrm{s}} = 0.05$ and $p_{\mathrm{d},1} = p_{\mathrm{d},2} = 0.475$ represent the membrane area of the soma and two dendrites, which are normalized by the total cell membrane area so that $p_{\mathrm{s}} + p_{\mathrm{d},1} + p_{\mathrm{d},2} = 1$. By construction, the activity of each dendritic compartment in isolation matched that of the single-compartment model. When the three compartments were coupled, random initial conditions were used for all compartments.

Reduced model and its nullclines. To analyze slow membrane oscillations underlying burst activity emerging through coactivation of I_{NMDA} and I_{DIC} (Fig. 2), we constructed a reduced model STN neuron. Since the Ca^{2+} time constant $\tau_{\mathrm{Ca}N}$ (80 ms) is relatively fast compared with the period of oscillation ($\sim$1.3 s) (Fig. 2*H*), we simply consider a case where $[\mathrm{Ca}]_N$ converges to its equilibrium value in *Eq. 5*: $[\mathrm{Ca}]_N = [\mathrm{Ca}]_{\infty}(V, h_N)(\equiv -k_1^N G_{\mathrm{NMDA}}(V, m_N, h_N)(V - V_{\mathrm{Ca}}))$. By using this simplification, we can obtain from *Eq. 1*, with the currents other than I_{leak}, I_{NMDA}, and I_{DIC} removed, and *Eq. 4* the following expressions:

$$C_{\mathrm{m}}\frac{\mathrm{d}V}{\mathrm{d}t} = -g_{\mathrm{l}}(V - V_{\mathrm{l}}) - g_D m_D^{\infty}\left\{[\mathrm{Ca}]_{\infty}(V, h_N)\right\} h_D (V - V_D) - G_{\mathrm{NMDA}}(V, m_N, h_N)(V - V_N) + I_{\mathrm{inj}}, \quad (10)$$

$$\frac{\mathrm{d}h_N}{\mathrm{d}t} = \frac{-h_N + h_N^{\infty}\left\{[\mathrm{Ca}]_{\infty}(V, h_N)\right\}}{\tau_{h_N}}. \quad (11)$$

These equations combined with *Eq. 7* constitute the reduced model that we will use for the analysis of NMDA- and DIC-dependent membrane oscillations. Note that I_{leak} does not contribute an additional variable to the model but does affect its quantitative performance, so we include it in the reduced model. We plotted the nullclines of this model, which are the curves of values where the velocity of each state variable equals 0 (see Fig. 7*B*). In the three-dimensional space spanned by V, h_N, and h_D, it is informative to plot the curved surface obtained from solving $\mathrm{d}V/\mathrm{d}t = 0$ from *Eq. 10* together with the curve obtained from simultaneously solving $\mathrm{d}h_N/\mathrm{d}t = 0$ and $\mathrm{d}h_D/\mathrm{d}t = 0$ from *Eqs. 7* and *11*:

$$\frac{\mathrm{d}V}{\mathrm{d}t} = 0 \Leftrightarrow h_D = \frac{-g_{\mathrm{l}}(V - V_{\mathrm{l}}) - G_{\mathrm{NMDA}}(V, m_N, h_N)(V - V_N) + I_{\mathrm{inj}}}{g_D m_D^{\infty}\left\{[\mathrm{Ca}]_{\infty}(V, h_N)\right\}(V - V_D)} \quad (12)$$

$$\frac{\mathrm{d}h_N}{\mathrm{d}t} = \frac{\mathrm{d}h_D}{\mathrm{d}t} = 0 \Leftrightarrow h_N = h_N^{\infty}\left\{[\mathrm{Ca}]_{\infty}(V, h_N)\right\},\ h_D = h_D^{\infty}(V). \quad (13)$$

We refer to the graphs of the solutions of *Eqs. 12* and *13* as the V-nullsurface and the h-nullcline, respectively. The nullsurface and nullcline were plotted and analyzed using MATLAB software.

RESULTS

NMDA-induced burst firing in STN neurons. The activation of the NMDA current and the DIC has been suggested to underlie NMDA-induced bursting in STN neurons (Zhu et al. 2005). To investigate how the interaction of these currents could lead to bursting, we constructed models of the NMDA current and the DIC that reproduce the voltage-dependent kinetics of these currents in in vitro recordings (Zhu et al. 2004, 2005; see METHODS and Fig. 1). The DIC in our model is rapidly activated by the Ca^{2+} influx evoked by the voltage-dependent NMDAR conductance and is slowly deinactivated through membrane hyperpolarization. Thus DIC is evoked most strongly when the membrane is depolarized to about -50 mV after being held at an initial hyperpolarizing potential (-100 mV; Fig. 1, *C–E*), as in Zhu et al. (2005), and this current exhibits its peak near the voltage at which the NMDA current takes its peak value (Fig. 1, *F* and *G*). The decay kinetics of DIC depends on the membrane potential, with longer durations

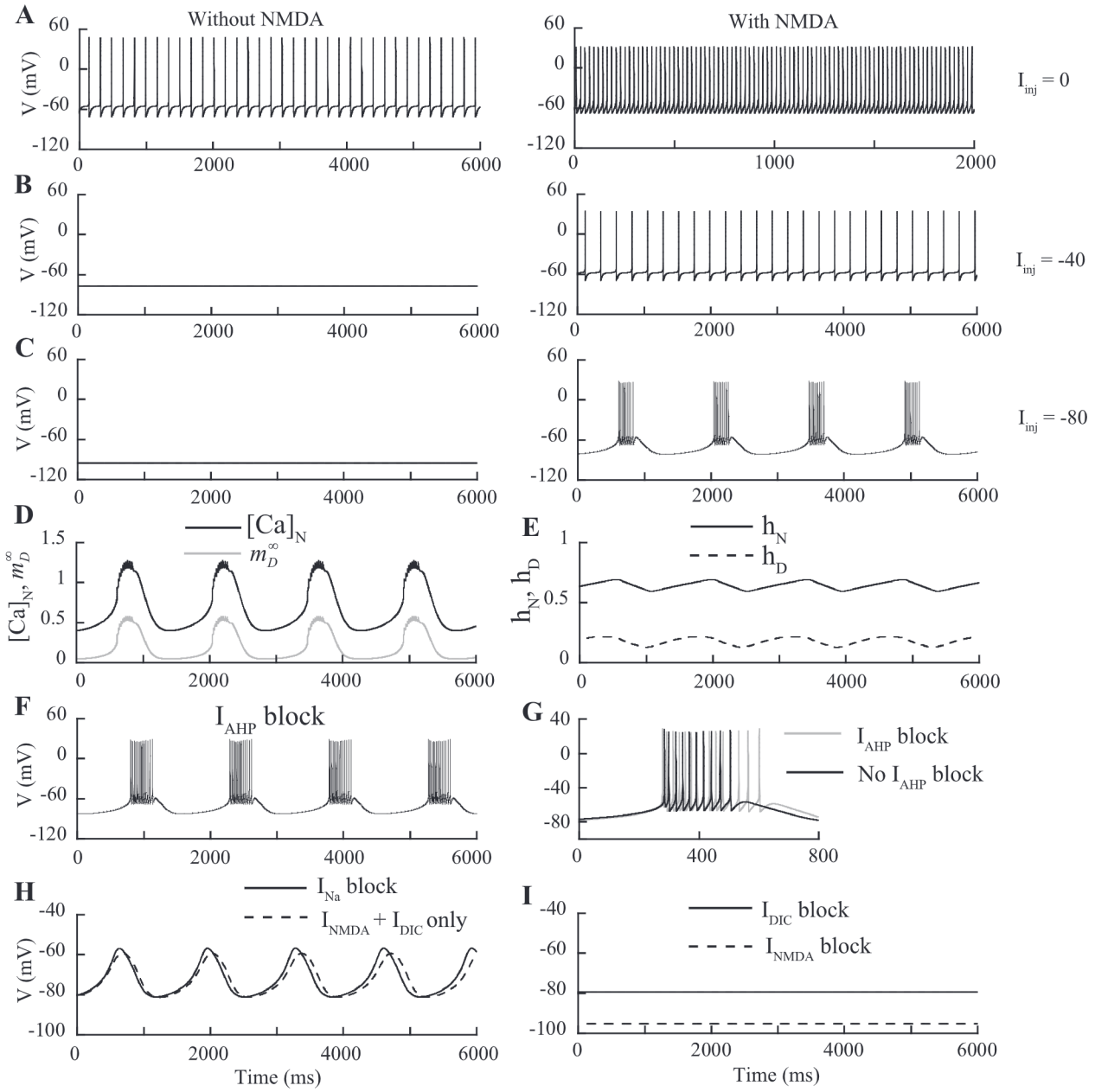

Fig. 2. Firing properties of the subthalamic nucleus (STN) model neuron. *A*: firing response of the model in the absence (*left*) or presence (*right*) of NMDA application [i.e., $m_N = 0$ (*left*) or 1 (*right*)] without hyperpolarizing current (I_{inj}) injection. *B*: model firing response with hyperpolarizing current of -40 μA/cm^2. *C*: model firing response with hyperpolarizing current of -80 μA/cm^2. *D*: time course of the NMDA-mediated Ca^{2+} concentration ($[Ca]_N$, black line) and that of the activation variable for DIC (m_D^∞, gray line) corresponding to burst firing. *E*: time courses of the inactivation variables for the NMDA current (h_N, solid line) and DIC (h_D, dashed line). *F*: firing profile of the model in the absence of AHP current (I_{AHP}; i.e., $g_{AHP} = 0$), with hyperpolarizing current of -80 μA/cm^2. *G*: burst duration becomes longer with the blockade of AHP (gray line) than in the presence of AHP (black line). *H*: slow membrane oscillation emerges under a blockade of Na^+ current ($g_{Na} = 0$; solid line) or with selective activation of DIC and NMDA currents ($g_{Na} = g_K = g_{Ca} = g_T = g_{AHP} = 0$; dashed line). *I*: blocking either DIC ($g_D = 0$; solid line) or NMDA current ($g_N = 0$; dashed line) eliminates the membrane oscillation and yields convergence to an equilibrium point. Parameter values are $g_N = 16.5$ mS/cm^2 and $g_D = 14$ mS/cm^2, except when NMDA or DIC is blocked, with hyperpolarizing current -80 μA/cm^2 for *D*–*I*.

occurring at moderate depolarization (about -60 mV; Fig. 1*E*; Zhu et al. 2005). However, we found that the details of its kinetics are not critical, since our key results (e.g., NMDA and hyperpolarization dependence of burstiness; see Figs. 2 and 3) do not change even when $\tau_D(V)$ (Fig. 1*B*), which determines the inactivation time course of DIC, is kept constant, at 300–700 ms, independent of membrane voltage (data not shown).

Incorporating the model NMDA current and DIC into a model STN neuron (Terman et al. 2002) yields NMDA-induced burst firing in the presence of hyperpolarizing inputs, which matches experimental observations (Fig. 2, *A*–*E*; Zhu et al. 2004). Without hyperpolarization, the neuron exhibits regular single-spike firing independent of whether NMDA is applied (Zhu et al. 2004), but the firing rate is much higher under NMDA application, which evokes depolarizing I_{NMDA} and I_{DIC} (Figs. 2*A* and 3*A*). With NMDA application, increased hyperpolarization decreases the firing rate and then increases it again for a wide range of g_N (Fig. 3*A*). This increased firing

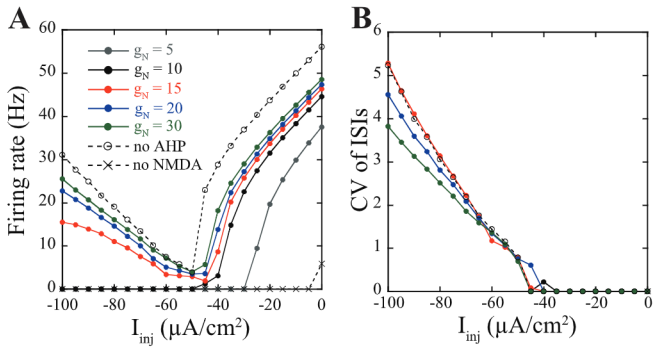

Fig. 3. Model STN neuron firing rate and regularity depend on the level of current injection and NMDA conductance. *A*: firing rate varies with injected current for NMDA peak conductance (g_N) of 5 (gray line), 10 (black line), 15 (red line), 20 (blue line), or 30 mS/cm^2 (green line). Open circles represent the case of no AHP current (with 20 mS/cm^2 NMDA conductance). Without NMDA, the model does not fire over most of the current range shown (curve with crosses becomes nonzero when injected current reaches -5 μA/cm^2). *B*: coefficient of variation (CV) of interspike intervals (ISIs) vs. injected current, with same color coding as in *A*. Note that, in the case of zero firing rate in *A*, there are no corresponding CV values plotted in *B*.

activity is accompanied by strong burstiness, featuring sequences of spikes on top of depolarizing plateaus alternating with periods of quiescence (Fig. 2*C*), which results in a higher coefficient of variation (CV) of interspike intervals (ISIs) (Fig. 3*B*). The dependence of NMDA-induced bursting on hyperpolarizing inputs is consistent with experimental results (Zhu et al. 2004) and reflects the voltage-dependent kinetics of DIC, which is deinactivated through hyperpolarization (Zhu et al. 2005; Fig. 1). Typical values of the interburst frequency (i.e., the frequency of occurrence of the active spiking phase) and intraburst frequency (i.e., the frequency of action potentials within each active phase), obtained at a high level of hyperpolarizing input ($I_{inj} = -80$ μA/cm^2; Fig. 2*C*, *right*), are 0.70 and 41 Hz, respectively. These particular frequencies exceed those reported by Zhu et al. (2004) (0.4 and 13.9 Hz, respectively), although the intraburst frequency is lower than that of some STN bursts arising in other conditions (e.g., Atherton et al. 2010, Bevan et al. 2002a), and the values observed can be significantly modified by the magnitude of the synaptic conductance and of the hyperpolarizing input (see below; Fig. 4).

The NMDA-induced bursting in the present model exhibits several characteristics that are observed in STN neurons (Zhu et al. 2004). Removal of I_T from the model, by setting $g_T = 0$ mS/cm^2, has essentially no effect on firing rate or on CVs of ISIs (data not shown). This finding agrees with the fact that mibefradil, a specific T-type Ca^{2+} channel blocker, does not significantly affect STN bursts (Zhu et al. 2004). Blocking I_{AHP} increases the burst duration (i.e., duration of active spiking phase within each burst) from the control value of 219.6 ms to 329.5 ms (relative change of 50.0%) and slightly decreases the interburst frequency, at $I_{inj} = -80$ μA/cm^2, from 0.70 Hz to 0.67 Hz (relative change of -3.9%) (Fig. 2, *F* and *G*). This result is similar to the experimentally observed effect of apamin on STN neurons, which considerably increases the duration of each burst without significantly altering the interburst frequency (Zhu et al. 2004). The blockade of I_{Na} in the presence of NMDA reveals a slow membrane oscillation (0.75 Hz) that underlies burst activity (Fig. 2*H*, solid line), as observed in STN neurons recorded in the presence of TTX (Zhu et al. 2004). A similar membrane oscillation occurs even when the active currents other than I_{NMDA} and I_{DIC} are removed (Fig. 2*H*, dashed line). However, blocking either of these two currents eliminates the slow oscillation (Fig. 2*I*),

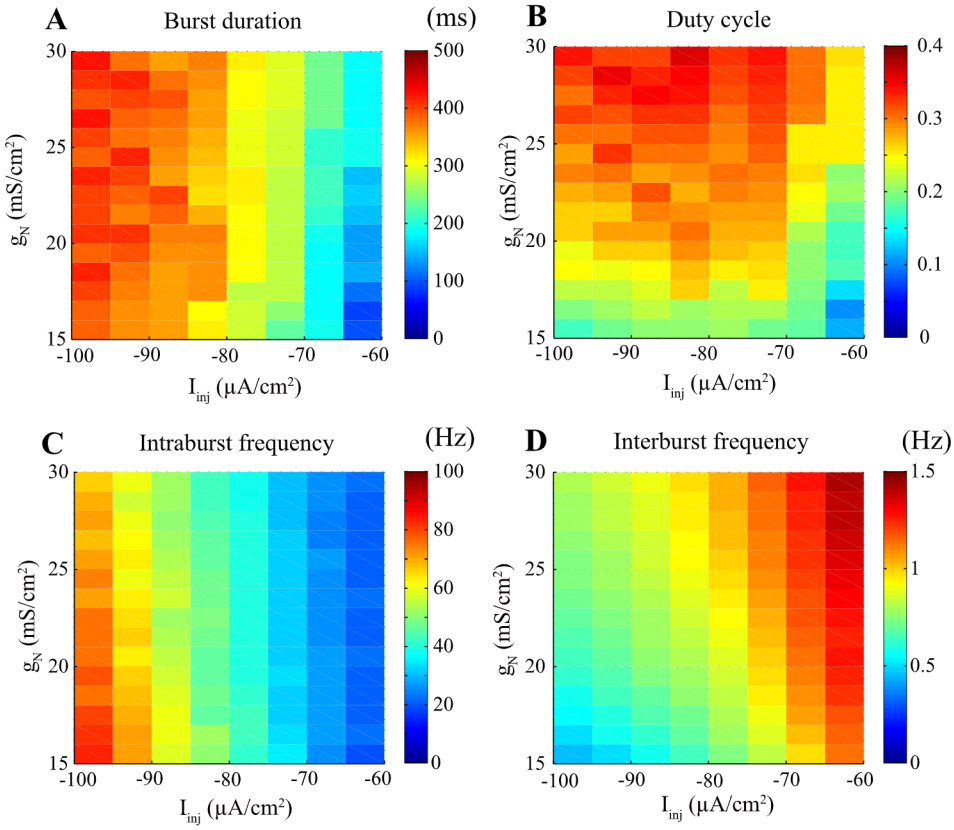

Fig. 4. Levels of hyperpolarization and NMDA activation significantly and differently regulate the quantitative properties of burst firing occurring in a dendritic compartment (i.e., single-compartment model). Burst duration (*A*), duty cycle (*B*), and intraburst (*C*) and interburst frequency (*D*) are plotted as functions of the injected current as well as the peak NMDA conductance.

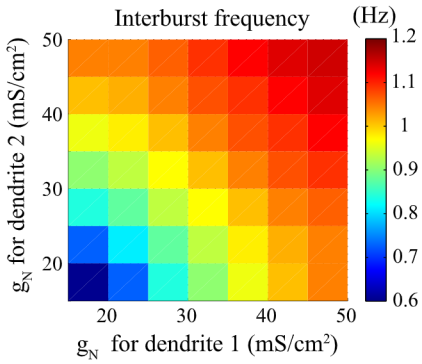

Fig. 5. Bursting oscillations in 2 dendritic compartments interact to control somatic burst frequency. The interburst frequency obtained using a 3-compartment model, consisting of 2 dendrites interacting with a soma, is plotted for various values of NMDA conductances in the 2 dendrites (as shown in the *x*- and *y*-axes) in the presence of hyperpolarizing inputs of -80 μA/cm^2. The peak conductance for DIC is fixed at 14 mS/cm^2 for both of the dendrites.

suggesting the involvement of the coactivation of I_{NMDA} and I_{DIC} in the membrane oscillation. This finding is consistent with the experimental observation that the NMDA-induced oscillation occurring during TTX treatment can be abolished by the effect of flufenamic acid, which blocks DIC (Zhu et al. 2004, 2005).

Dendritic interactions. Since NMDA channels are located at dendritic sites, we also simulated a three-compartment model consisting of two dendritic compartments coupled electrically to a common somatic compartment. In isolation, each of the three compartments were identical to the single-compartment model except that the NMDA current and DIC were included in the dendritic compartments but not the somatic one (see METHODS), and hence only the dendritic compartments exhibited bursting (Figs. 2 and 3).

Quantitative features of model bursts depend on its NMDA conductance, which could differ across different dendrites, as well as the injected current level. In a single dendritic compartment (equivalent to the single-compartment model), we computed burst duration (i.e., duration of active spiking phase within each burst), duty cycle (i.e., ratio of active phase duration to full burst period), intraburst spike frequency, and burst frequency as a function of these two parameters (Fig. 4, *A–D*, respectively). More hyperpolarizing current injections lead to prolonged burst durations and faster spiking within bursts (see also Fig. 3*A*). They also lower the overall burst frequency, leaving duty cycle relatively unaffected. In contrast, increases in g_N cause small changes in burst duration and intraburst frequency, relative to those induced by increases in hyperpolarizing inputs, but significantly increase burst frequency and duty cycle. Thus changes in dendritic NMDA conductances could be used to regulate these aspects of STN bursting.

We used the three-compartment model to test the interaction of dendritic oscillations at a soma not capable of generating bursts intrinsically. Simulations using dendritic parameter values associated with bursting in the single-compartment model, including a wide range of g_N values, yielded periodic bursting in the soma of the three-compartment model (Fig. 5), suggesting that a lack of burst-generating currents at the soma would not prevent transmission of bursts originating at the dendrites. Consistent with past results on bursting model cells coupled by gap junctions (De Vries et al. 1998; Smolen et al. 1993), the somatic burst frequency always fell between the intrinsic burst frequencies of the two dendrites when these were unequal (Fig. 5).

Analyzing the slow oscillation of the membrane potential. To explore the mechanism of I_{NMDA}- and I_{DIC}-dependent membrane oscillations underlying burst activity, we performed bifurcation analysis using a model that includes only the minimal set of currents required for the oscillatory behavior [i.e., $C_m(dV/dt) = -I_{leak} - I_{NMDA} - I_{DIC} + I_{inj}$; see Fig. 6]. We found that under an increase in the magnitude of hyperpolarizing inputs, a limit cycle oscillation arises from an equilibrium point via a supercritical Hopf bifurcation (Fig. 6, *B* and *C*), as can be expected from the occurrence of bursts with

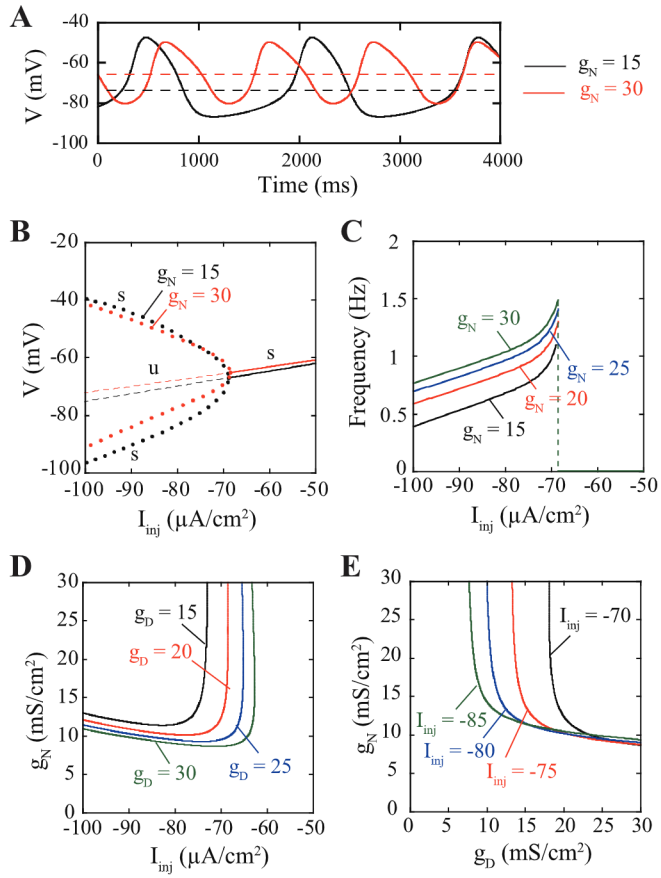

Fig. 6. Bifurcation analysis of the membrane potential oscillation. *A*: examples of the membrane potential oscillation for 2 different values of NMDA conductance, g_N = 15 (black line) or 30 mS/cm^2 (red line), with injected current of -85 μA/cm^2. Larger g_N augments the temporal average of the membrane potential (dashed lines; -74.0 and -66.0 mV for 15 and 30 mS/cm^2 conductances, respectively). *B*: membrane oscillation arises from a supercritical Hopf bifurcation when the hyperpolarizing current injection is strengthened. Filled circles represent the maximum and minimum values of membrane potential during oscillation, the lines (solid and dashed) show the equilibria, and the label of s (u) stands for stable (unstable) dynamics (NMDA conductance is color coded as in *A*). *C*: frequency of oscillation varies with injected current, as shown for 4 different NMDA conductances, g_N = 15 (black line), 20 (red line), 25 (blue line), or 30 mS/cm^2 (green line). *D*: Hopf bifurcation curves in the g_N vs. I_{inj} plane for DIC conductances, g_D = 15 (black line), 20 (red line), 25 (blue line), or 30 mS/cm^2 (green line). Oscillations arise for parameter values above and to the left of the curves. *E*: Hopf bifurcation curves in the g_N vs. g_D plane with hyperpolarizing current injection of -70 (black line), -75 (red line), -80 (blue line), or -85 μA/cm^2 (green line). Oscillations arise above and to the right of the curves.

strong hyperpolarization (Fig. 2, *A–C*). Larger hyperpolarization produced an increase in the amplitude and a decrease in the frequency of the membrane oscillation (Fig. 6, *B* and *C*), similar to experimental observations (Loucif et al. 2008). Although larger NMDAR conductances (g_N) decreased the amplitude of the oscillation, this change was accompanied by an elevation of the average membrane potential (Fig. 6, *A* and *B*), which would underlie the increased firing rate seen with larger g_N in Fig. 3*A*. Furthermore, the two-parameter bifurcation diagrams in Fig. 6, *D* and *E*, show that the occurrence of the limit cycle oscillation generally requires the combination of a sufficiently strong hyperpolarization, a sufficiently large g_N, and a sufficiently large g_D. This finding is consistent with the conditions under which burst firing occurs, as shown in Fig. 2. Additional two-parameter bifurcation analysis (data not shown) demonstrates that once I_{inj} is below some level (roughly -23 μA/cm^2), oscillations will occur, but they require the leak conductance g_l to be in the right range, and this range depends on the value of I_{inj}. More specifically, a transition from a stable rest state to stable oscillations happens as g_l is decreased, with the bifurcation occurring at a larger g_l as I_{inj} becomes more negative (e.g., the bifurcations in Fig. 6*B* occur with $I_{inj} \approx -70$ μA/cm^2 and $g_l = 2.25$ mS/cm^2). If g_l becomes too small, however, then oscillations are lost and a stable hyperpolarized rest state emerges; that is, enough leak current is needed to help pull the membrane potential up toward the leak reversal potential in the presence of a sufficiently strong hyperpolarizing injected current.

To further understand the oscillatory dynamics, we constructed a reduced three-dimensional model STN neuron (*Eqs. 7*, *10*, and *11*; see METHODS), which includes the membrane potential and the inactivation variables of the NMDA current and the DIC (h_N and h_D, respectively) as the state variables (Fig. 7*A*). We plotted the trajectory of the reduced model with its *V*-nullsurface and *h*-nullcline (*Eqs. 12* and *13*) in Fig. 7*B*, with parameters fixed at their values from the full model shown in Fig. 2*C*, *right*. The *V*-nullsurface has two fold curves (Fig. 7*B*, pink lines), at which the value of h_D takes a local maximum or minimum with respect to changes in *V*. As shown in Fig. 7*B*, when the model generates oscillations, the corresponding trajectory of the system (Fig. 7*B*, red and blue lines), starting from *point a*, slides up along the *V*-nullsurface until it reaches the fold curve at *point b*. At this moment, the variable *V* rapidly jumps and the trajectory rapidly transitions to *point c*, since the change in *V* is much faster than that of h_N and h_D, which are associated with slower desensitization processes. After that, the system slides down the *V*-nullsurface again as I_{DIC} inactivates, and at *point d*, it jumps to *point a*, thereby completing one oscillation.

For the oscillation to arise via the Hopf bifurcation, the equilibrium point where the *V*-nullsurface and *h*-nullcline (defined as the curve where the time derivatives of both h_N and h_D are 0) intersect (Fig. 7*B*, red cross) should lie between the two fold curves (Fig. 7*B*, pink lines) in a position where it is unstable (Izhikevich 2007). With parameters tuned to this regime and the neuron starting in a sufficiently hyperpolarized state that I_{DIC} is deinactivated (Fig. 1), the application of NMDA activates I_{NMDA}, and this effect in turn activates I_{DIC} through NMDAR-mediated Ca^{2+} influx. However, since I_{NMDA} is an inward current in this voltage range, it is not obvious why its activation alone is not sufficient to elicit membrane oscillations and, instead, the concurrent activation of the DIC is required in both the model (Fig. 6*E*) and the experiments (Zhu et al. 2004). To explain this observation, we plotted the changes in the amplitudes of I_{NMDA} and I_{DIC} and their sum at the equilibrium point of the reduced model as one of the parameters g_N or g_D was varied and the other was kept at a relatively small fixed value (Fig. 8, *A* and *B*). We found that increasing g_N produces saturation of I_{NMDA} through the Ca^{2+}-dependent desensitization (*Eq. 4*) and thereby causes the saturation of I_{DIC} (Fig. 8*A*). On the other hand, increasing g_D yields saturation of I_{NMDA} but not of I_{DIC} (Fig. 8*B*). This is because increases in g_D directly amplify I_{DIC}, even though NMDA saturation disables further enhancement of NMDAR-

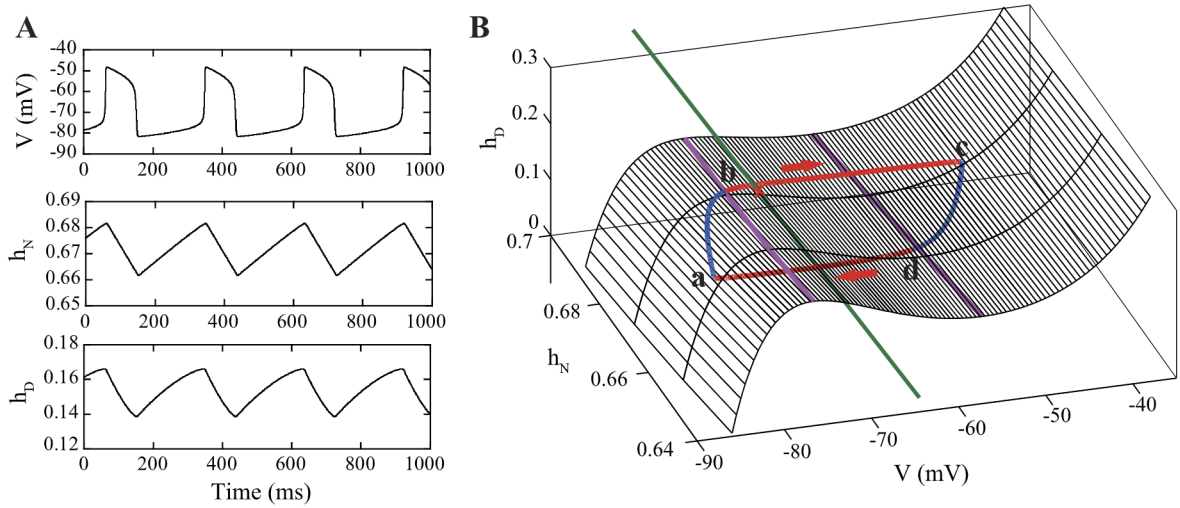

Fig. 7. Reduced model dynamics. *A*: time course of reduced model voltage (*top*), NMDA current inactivation (*middle*), and DIC current inactivation (*bottom*). *B*: nullclines of the reduced model and an oscillatory trajectory in the reduced model's 3-dimensional phase space. The *h*-nullcline (green line) intersects with the *V*-nullsurface (black) at a point denoted by a red cross (i.e., equilibrium point). Pink lines show the fold curves on the *V*-nullsurface, where the DIC inactivation variable achieves local extrema with respect to *V*. Blue and red curves show the oscillatory trajectory corresponding to *A*. The blue and red curves are used, respectively, to represent the points where the trajectory is located very near to the *V*-nullsurface and excursions along which the trajectory jumps from one neighborhood of the *V*-nullsurface to another neighborhood of it. Parameter values are $g_N = 16.5$ mS/cm^2, $g_D = 14$ mS/cm^2, and $I_{inj} = -80$ μA/cm^2.

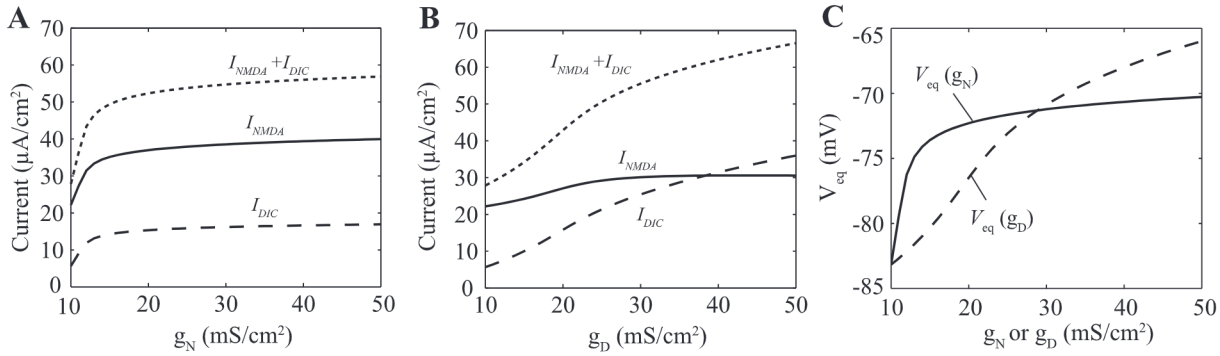

Fig. 8. Features of the reduced model at equilibrium. *A*: NMDA current (solid line), DIC (dashed line), and their sum (dotted line), obtained at the equilibrium state of the reduced model, as a function of NMDA conductance. *B*: same currents as a function of DIC conductance. *C*: membrane potential at the equilibrium state (V_{eq}) plotted against NMDA conductance (solid line) and DIC conductance (dashed line). Parameter values are $g_D = 10$ mS/cm^2 in *A* and *C*, $g_N = 10$ mS/cm^2 in *B* and *C*, and $I_{inj} = -80$ μA/cm^2.

mediated Ca^{2+} influx, as can be expected from *Eq. 6*. Therefore, the depolarizing input provided by I_{NMDA} and I_{DIC} can be enhanced more, yielding a larger equilibrium value of membrane potential (V_{eq}), through increases in g_D than by increases in g_N (Fig. 8*C*). In particular, a sufficiently large g_D is required to push V_{eq} through the Hopf bifurcation (e.g., compare Figs. 7*B* and 8*C*) and achieve oscillations (assuming that g_l is in the appropriate range, as in the reduced model analyzed in Fig. 6). In summary, to obtain oscillations, the NMDA current is required to activate the DIC, and the DIC must be sufficiently strong to destabilize the low-voltage rest state associated with the hyperpolarizing current injection.

DISCUSSION

STN neurons mostly exhibit irregular tonic spiking in normal conditions, whereas parkinsonism in patients and experimental models is characterized by an increased prevalence of oscillations and bursting and higher overall firing rates in STN (Bergman et al. 1994; Brown et al. 2001; Gatev et al. 2006; Levy et al. 2001; Magnin et al. 2000; Mallet et al. 2008). To explore one possible mechanism for bursting in STN neurons, we have extended a previously published conductance-based computational model for STN neuron activity (Terman et al. 2002), calibrated to rodent slice data, to include additional currents subsequently observed and characterized in rat brain slice (Zhu et al. 2005). When parameters associated with these currents are fit to experimental data, the resulting model generates robust bursting oscillations under a constant hyperpolarizing current injection and complete NMDA activation. Moreover, this bursting activity responds to manipulations representing the application of apamin or of TTX in a way that is consistent with experimental results (Zhu et al. 2004). Interestingly, the bursting oscillations observed in the model, given sustained NMDA current activation, arise predominantly from repeated cycles of activation of a nonspecific cationic current, I_{DIC}, by Ca^{2+} influx through NMDA channels, followed by voltage-dependent inactivation of I_{DIC}. Although a small amount of slow, Ca^{2+}-dependent NMDA desensitization (Krupp et al. 1996; Monyer et al. 1994) waxes and wanes during the oscillations, no additional elements are needed for this bursting activity to occur. This oscillation mechanism is similar to that arising in previous modeling of the interaction of NMDA current and an outward Na^+-pump current (Li et al. 1996), but it was not obvious that the specific combination of current magnitudes and kinetics identified experimentally in STN neurons would yield such oscillations, as our work shows.

Our model extends an earlier published model (Terman et al. 2002) to include the NMDA and DIC currents hypothesized by Zhu et al. (2004, 2005) to contribute to this form of STN bursting activity. Therefore, our model can still reproduce the characteristic firing properties of STN cells shown in the original model (Terman et al. 2002), such as the intrinsic spontaneous discharge and postinhibitory rebound bursting (Bevan and Wilson 1999; Bevan et al. 2000), which depends on T-type Ca^{2+} currents. Other currents identified in STN neurons (Atherton et al. 2010; Barraza et al. 2009; Beurrier et al. 1999; Gillies and Willshaw 2006; Hahn and McIntyre 2010; Overton et al. 1995; Nakanishi et al. 1987) were omitted to maintain a focus on a specific putative burst mechanism, and our results suggest that these additional currents are not necessary for the experimentally observed STN bursting to occur, although they may affect its properties. In particular, we omit HCN currents that have been identified in STN neurons (Atherton et al. 2010), since they are activated by synaptic inhibition and act by limiting the availability of low-threshold T-type Ca^{2+} current, neither of which is an important feature in our study. Zhu et al. (2004) provided evidence that a variety of voltage-dependent Ca^{2+} currents are not significantly involved in STN bursting, justifying their omission from our model for this particular study. Loucif et al. (2005) observed a significant increase in robustness of bursting when NMDA application was supplemented by apamin administration, a finding that we have not attempted to explain with our model, yet this result was obtained without strong membrane hyperpolarization, and thus its relation to our model is not clear. With membrane hyperpolarization, Zhu et al. (2004) showed that apamin application lengthened bursts and interburst intervals but did not qualitatively alter bursting, and our simulations agree with these results. Beyond apamin, additional K^+ currents (Barraza et al. 2009) may contribute to burst characteristics, and the effects of these currents may help explain why the bursts we observed were briefer (0.22 vs. 1.8 s) and faster (0.7 vs. 0.4 Hz) than those reported by Zhu et al. (2004). Drastic reductions of bath K^+ concentrations were found to increase burst durations and to enhance the amplitude of membrane potential hyperpolarizations between bursts, supporting the involvement of K^+ currents in the observed bursting, although effects of K^+

reductions on interburst interval durations were not reported (Zhu et al. 2004).

The bursting that we have studied occurred experimentally under combined hyperpolarizing current injection and NMDA bath application. These are rather extreme conditions, and their relevance to parkinsonian states in vivo depends on whether or not STN cells are subjected to significant sources of hyperpolarization and NMDA inputs in that setting. In parkinsonian conditions, STN neurons do experience bouts of strong inhibitory inputs from GPe neurons (Baufreton et al. 2001, 2005; Bevan et al. 2002a, 2002b; Terman et al. 2002). In STN neurons that are voltage clamped at −60 mV, Baufreton et al. (2001) observed hyperpolarizing currents of 117 ± 14 μA/cm^2 induced by application of the GABA agonist muscimol at 10 μM (with half-maximal response at 5.2 μM), suggesting that the currents injected to induce the bursting that we have discussed are of physiologically relevant amplitudes (but see Loucif et al. 2005). Dopamine depletion, a key feature of parkinsonism, is also known to lead directly to hyperpolarized STN membrane potentials (Cragg et al. 2004, Loucif et al. 2008), and the absence of dopamine enhances GABA-mediated outward currents (Shen and Johnson 2005), suggesting that the loss of dopamine associated with parkinsonism may help promote the hyperpolarization that can serve as a backdrop for STN bursting. Consistent with this idea, Loucif et al. (2008) found that STN burst firing that is induced in slices by NMDA and apamin administration can be switched to tonic, regular firing by dopamine application. These forms of hyperpolarization would not match the intensity of sustained hyperpolarization achieved by experimental current injection, however, and simulation studies of how these effects can contribute to bursting are still needed.

Positing that membrane hyperpolarization is an important component of STN bursting leads to the prediction that countering STN hyperpolarization may be therapeutic for parkinsonism. This prediction should not be interpreted as a prescription for elimination of sources of inhibition to STN, however. Lesions in GPe neurons of 1-methyl-4-phenyl-1,2,3,6-tetrahydropyridine (MPTP)-treated monkeys have been found to worsen parkinsonian symptoms (Zhang et al. 2006). Complete elimination or block of GPe activity after the induction of a dopamine-depleted state could yield such effects by promoting at least somewhat excessive STN firing as well as reduced inhibition to GPi neurons (leading to enhanced GPi firing as also reported in Zhang et al. 2006), even if it did reduce STN bursting, effectively substituting one form of pathology for another. On the other hand, less extreme interventions that lower the levels of inhibition to STN more modestly would be expected to reduce bursting without such negative side effects.

As for the activation of STN NMDA receptors, although it was found that the ratio of AMPA current to NMDA current was significantly increased by 6-hydroxydopamine (6-OHDA) lesions in rats, NMDA currents remain strong after lesions, with the ratio near one (Shen and Johnson 2005). A natural source for NMDA activation is the delivery of cortical glutamatergic inputs to STN via the hyperdirect pathway, and cortical stimulation is indeed known to elicit STN responses (Magill et al. 2004a). Experiments show that slow cortical oscillations in anesthetized rats are associated with and temporally coupled with enhanced STN bursting and that peaks in STN bursting and cortical oscillations are nearly coincident in this setting (Magill et al. 2001, 2004b). Furthermore, dopamine depletion strengthened the cortical influence on STN activity, whereas STN bursting in these experiments was eliminated by cortical ablation (Magill et al. 2001). Of course, cortically induced NMDA activation would not match the sustained activation from experimental bath application of NMDA, and these more physiological mechanisms remain to be explored computationally. Interestingly, the administration of various NMDA antagonists, such as amantadine and memantine, yields improvements in motor signs in Parkinson's disease patients (Blandini et al. 2001; Metman et al. 1998; Varanese et al. 2010). Experiments have also been done to investigate how particular NMDA antagonists affect NMDA currents in parkinsonian conditions. In extracellular recordings in 6-OHDA rats, the NMDA antagonist MK801 did not significantly modify the incidence of 3- to 8-Hz oscillations but did decrease spectral power in this frequency range (Allers et al. 2005). Furthermore, coapplication of a dopamine D1 receptor agonist eliminated all bursting, consistent with the idea that a weak dopamine signal together with strong NMDA currents supports STN bursting. In contrast, amantadine significantly increased firing rates but had surprisingly little effect on bursting in lesioned animals, although it eliminated 3- to 8-Hz oscillations in intact animals (Allers et al. 2005). Clearly, additional experiments are needed to sort out the changes in NMDA currents that occur under parkinsonian conditions and how these changes impact STN activity patterns.

APPENDIX: DESCRIPTION OF ACTIVE CURRENTS OTHER THAN I_{NMDA} AND I_{DIC}

As mentioned in METHODS, with the exception of I_{NMDA} and I_{DIC}, the currents in *Eq. 1* have been taken from a previous model (Terman et al. 2002). These currents are described as $I_{Na} = g_{Na}m_\infty^3(V)h(V - V_{Na})$, $I_K = g_K n^4(V - V_K)$, $I_T = g_T a_\infty^3(V)b_\infty^2(r)(V - V_{Ca})$, $I_{Ca} = g_{Ca}s_\infty^2(V)(V - V_{Ca})$, and $I_{AHP} = g_{AHP}(V - V_K)\{[Ca]_{AHP}/([Ca]_{AHP} + k_1)\}$. The gating variables n, h, and r obey first-order kinetics of the form $dX/dt = \phi_X\{[X_\infty(V) - X]/\tau_X(V)\}$ with $\tau_X(V) = \tau_X^0 + \tau_X^1/\{1 + \exp[(V - \theta_X^\tau)/\sigma_X^\tau]\}$ (where X can be n, h, or r). For all the gating variables, the voltage dependence at steady state is specified as $X_\infty(V) = 1/\{1 + \exp[(V - \theta_X)/\sigma_X]\}$ (where X can be n, m, h, r, a, or s). For the inactivation variable b, the steady-state value is given by $b_\infty(r) = 1/\{1 + \exp[(r - \theta_b)/\sigma_b]\} - 1/[1 + \exp(-\theta_b/\sigma_b)]$. The Ca^{2+} signal involved in the activation of I_{AHP} is governed by $d[Ca]_{AHP}/dt = \varepsilon(-I_{Ca} - I_T - k_{Ca}[Ca]_{AHP})$. We assume that this Ca^{2+} signal, which is mediated by voltage-dependent Ca^{2+} channels, is independent from that associated with the activation of I_{DIC}, which is mediated by NMDA channels (Zhu et al. 2005). The parameter values used are as follows [values in parentheses show those used in Terman et al. (2002) for the cases where the values are modified from the original ones]: $g_{Na} = 37.5$ mS/cm^2, $g_K = 45$ mS/cm^2, $g_{AHP} = 20$ mS/cm^2 (9 mS/cm^2), $g_{Ca} = 0.5$ mS/cm^2, $g_T = 0.1$ mS/cm^2 (0.5 mS/cm^2), $V_{Na} = 55$ mV, $V_K = -80$ mV, $\theta_m = -30$ mV, $\sigma_m = -14.5$ mV (−15.0 mV), $\theta_h = -39$ mV, $\sigma_h = 3.1$ mV, $\theta_n = -32$ mV, $\sigma_n = -8$ mV, $\theta_r = -67$ mV, $\sigma_r = 2$ mV, $\theta_a = -63$ mV, $\sigma_a = -7.8$ mV, $\theta_b = 0.4$ mV, $\sigma_b = -0.1$ mV, $\theta_s = -39$ mV, $\sigma_s = -8$ mV, $\tau_h^0 = 1$ ms, $\tau_h^1 = 500$ ms, $\theta_h^\tau = -85$ mV (−57 mV), $\sigma_h^\tau = 3$ mV, $\tau_n^0 = 1$ ms, $\tau_n^1 = 100$ ms, $\theta_n^\tau = -80$ mV, $\sigma_n^\tau = 26$ mV, $\tau_r^0 = 40$ ms, $\tau_r^1 = 17.5$ ms, $\theta_r^\tau = 68$ mV, $\sigma_r^\tau = 2.2$ mV, $\phi_h = \phi_n = 0.75$, $\phi_r = 0.2$, $k_1 = 7.5$ μM (15 μM), $\varepsilon = 3.75 \times 10^{-5}$ mM·s^{-1}(μA·cm^{-2})$^{-1}$, and $k_{Ca} = 22.5$ μA·cm^{-2}·μM^{-1}.

ACKNOWLEDGMENTS

We thank P. Magill and I. Stanford for discussions that were essential to the initiation of this work as well as for reading and providing comments on this manuscript and R. Turner for reading and commenting on a draft of this work.

GRANTS

S. Kubota was partially supported by the Program to Accelerate the Internationalization of University Education from the Japanese government and the International Research Training Program from Yamagata University. J. Rubin received support from National Science Foundation Awards DMS 0716936 and DMS 1021701.

DISCLOSURES

No conflicts of interest, financial or otherwise, are declared by the author(s).

REFERENCES

Allers KA, Bergstrom DA, Leyla JG, Kreiss DS, Walters JR. MK801 and amantadine exert different effects on subthalamic neuronal activity in a rodent model of Parkinson's disease. *Exp Neurol* 191: 104–118, 2005.

Atherton JF, Kitano K, Baufreton J, Fan K, Wokosin D, Tkatch T, Shigemoto R, Surmeier DJ, Bevan MD. Selective participation of somatodendritic HCN channels in inhibitory but not excitatory synaptic integration in neurons of the subthalamic nucleus. *J Neurosci* 30: 16025–16040, 2010.

Barraza D, Kita H, Wilson CJ. Slow spike frequency adaptation in neurons of the rat subthalamic nucleus. *J Neurophysiol* 102: 3689–3697, 2009.

Baufreton J, Garret M, Dovero S, Dufy B, Bioulac B, Taupignon A. Activation of GABAA receptors in subthalamic neurons in vitro: properties of native receptors and inhibition mechanisms. *J Neurophysiol* 86: 75–85, 2001.

Baufreton J, Atherton JF, Surmeier J, Bevan MD. Enhancement of excitatory synaptic integration by GABAergic inhibition in the subthalamic nucleus. *J Neurosci* 25: 8505–8517, 2005.

Bergman H, Wichmann T, Karmon B, DeLong MR. The primate subthalamic nucleus. II. Neuronal activity in the MPTP model of parkinsonism. *J Neurophysiol* 72: 507–520, 1994.

Beurrier C, Cognar P, Biolac B, Hammond C. Subthalamic nucleus neurons switch from single-spike activity to burst-firing mode. *J Neurosci* 19: 599–609, 1999.

Beurrier C, Biolac B, Hammond C. Slowly inactivating sodium current (I_{NaP}) underlies single-spike activity in rat subthalamic nucleus neurons. *J Neurophysiol* 83: 1951–1957, 2000.

Bevan MD, Magill PJ, Hallworth NE, Bolam JP, Wilson CJ. Regulation of the timing and pattern of action potential generation in rat subthalamic neurons in vitro by GABA-A IPSPs. *J Neurophysiol* 87: 1348–1362, 2002a.

Bevan MD, Magill PJ, Terman D, Bolam JP, Wilson CJ. Move to the rhythm: oscillations in the subthalamic nucleus-external globus pallidus network. *Trends Neurosci* 25: 525–531, 2002b.

Bevan MD, Wilson CJ. Mechanisms underlying spontaneous oscillation and rhythmic firing in rat subthalamic neurons. *J Neurosci* 19: 7617–7628, 1999.

Bevan MD, Wilson CJ, Bolam JP, Magill PJ. Equilibrium potential of $GABA_A$ current and implications for rebound burst firing in rat subthalamic neurons in vitro. *J Neurophysiol* 83: 3169–3172, 2000.

Blandini F, Greenamyre JT, Fancellu R, Nappi G. Blockade of subthalamic glutamatergic activity corrects changes in neuronal metabolism and motor behavior in rats with nigrostriatal lesions. *Neurol Sci* 22: 49–50, 2001.

Brown P, Oliviero A, Mazzone P, Insola A, Tonali P, Di Lazzaro V. Dopamine dependency of oscillations between subthalamic nucleus and pallidum in Parkinson's disease. *J Neurosci* 21: 1033–1038, 2001.

Cragg SJ, Baufreton J, Xue Y, Bolam JP, Bevan MD. Synaptic release of dopamine in the subthalamic nucleus. *Eur J Neurosci* 20:1788–1802, 2004.

De Vries G, Sherman A, Zhu HR. Diffusively coupled bursters: effects of cell heterogeneity. *J Math Biol* 60: 1167–1200, 1998.

Ermentrout B. *Simulating, Analyzing, and Animating Dynamical Systems. A Guide to XPPAUT for Researchers and Students*. Philadelphia, PA: Soc Indus Appl Math, 2002.

Feger J, Hassanoi OK, Moroux M. The subthalamic nucleus and its connections. *Adv Neurol* 74: 31–43, 1997.

Gatev P, Darbin O, Wichmann T. Oscillations in the basal ganglia under normal conditions and movement disorders. *Mov Disord* 21: 1566–1577, 2006.

Gillies A, Willshaw D. Membrane channel interactions underlying rat subthalamic projection neuron rhythmic bursting activity. *J Neurophysiol* 95: 2352–2365, 2006.

Hahn PJ, McIntyre CC. Modeling shifts in the rate and pattern of subthalamopallidal network activity during deep brain stimulation. *J Comput Neurosci* 28: 425–441, 2010.

Izhikevich EM. *Dynamical Systems in Neuroscience*. Cambridge: MIT Press, 2007.

Jahr CE, Stevens CF. Voltage dependence of NMDA-activated macroscopic conductances predicted by single-channel kinetics. *J Neurosci* 10: 3178–3182, 1990.

Krupp JJ, Vissel B, Heinemann SF, Westbrook GL. Calcium-dependent inactivation of recombinant *N*-methyl-D-aspartate receptors is NR2 subunit specific. *Mol Pharmacol* 50: 1680–1688, 1996.

Levy R, Lang AE, Dostrovsky JO, Pahapill P, Romas J, Saint-Cyr J, Hutchison WD, Lozano AM. Lidocaine and muscimol injections in subthalamic nucleus reverse parkinsonian symptoms. *Brain* 124: 2105–2118, 2001.

Li YX, Bertram R, Rinzel J. Modeling *N*-methyl-D-aspartate-induced bursting in dopamine neurons. *Neuroscience* 71: 397–410, 1996.

Loucif AJ, Woodhall GL, Sehirli US, Stanford IM. Depolarisation and suppression of burst firing activity in the mouse subthalamic nucleus by dopamine D1/D5 receptor activation of a cyclic-nucleotide gated non-specific cation conductance. *Neuropharmacology* 55: 94–105, 2008.

Loucif KC, Wilson CL, Baig R, Lacey MG, Stanford IM. Functional interconnectivity between the globus pallidus and the subthalamic nucleus in the mouse brain slice. *J Physiol* 567: 977–987, 2005.

Magill PJ, Bolam PJ, Bevan MD. Dopamine regulates the impact of the cerebral cortex on the subthalamic nucleus-globus pallidus network. *Neuroscience* 106: 313–330, 2001.

Magill PJ, Sharott A, Bolam JP, Brown P. Synchronous unit activity and local field potentials evoked in the subthalamic nucleus by cortical stimulation. *J Neurophysiol* 92: 700–714, 2004a.

Magill PJ, Sharott A, Bolam JP, Brown P. Brain state-dependency of coherent oscillatory activity in the cerebral cortex and basal ganglia of the rat. *J Neurophysiol* 92: 2122–2138, 2004b.

Magnin M, Morel A, Jeanmonod D. Single-unit analysis of the pallidum, thalamus, and subthalamic nucleus in parkinsonian patients. *Neuroscience* 96: 549–564, 2000.

Mallet N, Pogosyan A, Sharott A, Csicsvari J, Bolam JP, Brown P, Magill PJ. Disrupted dopamine transmission and emergence of exaggerated beta oscillations in subthalamic nucleus and cerebral cortex. *J Neurosci* 28: 4795–4806, 2008.

Metman LV, Dotto PD, van den Munckhof P, nFang J, Mouradian MM, Chase TN. Amantadine as treatment for dyskinesias and motor fluctuations in Parkinson's disease. *Neurology* 50: 1323–1326, 1998.

Monyer H, Burnashev N, Laurie DJ, Sakmann B, Seeburg PH. Developmental and regional expression in the rat brain and functional properties of four NMDA receptors. *Neuron* 12: 529–540, 1994.

Nakanishi H, Kita H, Kitai ST. Electrical membrane properties of rat subthalamic nucleus neurons in an in vitro slice preparation. *Brain Res* 437: 35–44, 1987.

Nambu A, Takada M, Inase M, Tokuno H. Dual somatotopical representations in the primate subthalamic nucleus: evidence for ordered but reversed body-map transformations from the primary motor cortex and the supplementary motor area. *J Neurosci* 16: 2671–2683, 1996.

Nambu A, Tokuno H, Takada M. Functional significance of the cortico-subthalamo-pallidal 'hyperdirect' pathway. *Neurosci Res* 43: 111–117, 2002.

Overton PG, Greenfield SA. Determinant of neuronal firing pattern in the guinea-pig subthalamic nucleus: an in vivo and in vitro comparison. *J Neural Transm Park Dis Dement Sect* 10: 41–54, 1995.

Plenz D, Kital S. A basal ganglia pacemaker formed by the subthalamic nucleus and external globus pallidus. *Nature* 400: 677–682, 1999.

Rouzaire-Dubois B, Scarnati E. Pharmacological study of the cortical-induced excitation of subthalamic nucleus neurons in the rat: evidence for amino acids as putative neurotransmitters. *Neuroscience* 21: 429–440, 1987.

Shen KZ, Johnson SW. Dopamine depletion alters responses to glutamate and GABA in the rat subthalamic nucleus. *Neuroreport* 16: 171–174, 2005.

Smith Y, Bevan MD, Shink E, Bolam JP. Microcircuitry of the direct and indirect pathways of the basal ganglia. *Neuroscience* 86: 353–387, 1998.

Smolen P, Rinzel J, Sherman A. Why pancreatic islets burst but single beta cells do not: the heterogeneity hypothesis. *Biophys J* 64: 1668–1680, 1993.

Standaert DG, Testa CM, Young AB, Penney JB. Organization of *N*-Methyl-D-aspartate glutamate receptor gene expression in the basal ganglia of the rat. *J Comp Neurol* 343: 1–16, 1994.

Terman D, Rubin JE, Yew AC, Wilson CJ. Activity patterns in a model for the subthalamopallidal network of the basal ganglia. *J Neurosci* 22: 2963–2976, 2002.

Varanese S, Howard J, Rocco AD. NMDA antagonist memantine improves levodopa-induced dyskinesias and "on-off" phenomena in Parkinson's disease. *Mov Disord* 25: 508–510, 2010.

Wenzel A, Villa M, Mohler H, Benke D. Developmental and regional expression of NMDA receptor subtypes containing the NR2D subunit in rat brain. *J Neurochem* 66: 1240–1248, 1996.

Zhang J, Russo G, Mewes K, Rye B, Vitek J. Lesions in monkey globus pallidus extremus exacerbate parkinsonian symptoms. *Exp Neurol* 199: 446–453, 2006.

Zhu ZT, Munhall A, Shen KZ, Johnson SW. Calcium-dependent subthreshold oscillations determine bursting activity induced by *N*-methyl-D-aspartate in rat subthalamic neurons in vitro. *Eur J Neurosci* 19: 1296–1304, 2004.

Zhu ZT, Munhall A, Shen KZ, Johnson SW. NMDA enhances depolarization-activated inward current in subthalamic neurons. *Neuropharmacology* 49: 317–327, 2005.